Electronic Supplementary Information

*for*

# Enhancing oxygen evolution performances of NiO-based electrocatalysts through synergistic plasma processing and laser treatment

Davide Barreca,*[a] Alessandro Bellucci,[b] Matteo Mastellone,[c] Daniele Maria Trucchi,[b] Chiara Maccato,[a,d] Ermanno Pierobon,[d] Alberto Gasparotto,[a,d] and Gian Andrea Rizzi[a,d]

[a] CNR-ICMATE and INSTM, Department of Chemical Sciences, Padova University, 35131 Padova, Italy.

[b] CNR-ISM, Sez. Montelibretti, DiaTHEMA Lab, 00010 Montelibretti (RM), Italy.

[c] CNR-ISM, Sez. Tito Scalo, 85050 Tito Scalo (PZ), Italy.

[d] Department of Chemical Sciences, Padova University and INSTM, 35131 Padova, Italy.

* Corresponding author; e-mail: davide.barreca@cnr.it.

# Table of Contents

## *§ S1. Experimental*

### *§ S1-1. Plasma-assisted CVD of NiO nanostructures*

The growth of NiO nanostructures was performed on pre-cleaned[1, 2] fluorine-doped tin oxide (FTO)-coated glass substrates (Aldrich®; FTO thickness ≈600 nm; ≈7 $\Omega \times sq^{-1}$) using a custom-built two-electrode plasma assisted-chemical vapor deposition (PA-CVD) apparatus.[3] The substrates were mounted on the surface of the grounded electrode, whereas radio frequency (RF; 13.56 MHz) was delivered to a second electrode (electrode diameter = 9 cm; inter-electrode distance = 6 cm). In a typical deposition experiment, (0.15 ± 0.01) g of the precursor powders [$Ni(tfa)_2TMEDA$;[4, 5] tfa = 1,1,1-trifluoro-2,4-pentanedionate; TMEDA = *N*,*N*,*N*′,*N*′-tetramethylethylenediamine), loaded in an external glass vessel, were heated at 75°C by means of an oil bath, and the vapors were transported into the reactor by electronic grade Ar [flow rate = 60 standard cubic centimeters per minute (sccm)]. In order to prevent undesired precursor condensation phenomena, connection gas lines were kept at 150°C by means of external heating tapes. Two independent gas lines were used to introduce electronic grade Ar and $O_2$ (flow rates = 15 and 5 sccm, respectively) directly into the reaction chamber. Based on preliminary optimization experiments, growth processes were performed at substrate temperatures of 200, 300, and 400°C, for a total duration of 90 min (total pressure = 1.0 mbar; RF power = 20 W).

### *§ S1-2. Laser treatments*

Surface treatments were performed using a Ti-Sapphire femtosecond laser (Spectra-Physics, λ = 800 nm) with linear polarization, pulse duration of 100 fs, and repetition rate (*f*) of 1 kHz. The laser system utilizes mode-locked oscillation to generate ultrashort pulses, ensuring a precise and high-energy delivery. Since the initial pulse energy is low, a regenerative amplifier increases the pulse energy while preserving its temporal profile.

The specimens were mounted on a nanometric-resolution movement stage (μFAB station, Newport), and the laser beam was focused perpendicularly onto the sample using a 4× magnification objective lens. The treatment was conducted in air using a scanning mode, where the sample moves relative to the laser beam. In this way, the number of overlapping pulses per unit area (*N*) is determined by the scanning speed (*v*) as:

$$N = 2r \times f / v \tag{S1}$$

where $2r$ is the laser spot diameter and $f$ is the repetition rate. The laser scans the surface line by line, moving from left to right before shifting to the next line below, systematically covering the entire sample area.

To optimize the processing parameters for the full specimen area, a series of preliminary experiments was conducted by varying the number of impinging pulses. This variation allowed to obtain different accumulated pulse fluence ($\Phi_{acc}$) values, defined as:

$$\Phi_{acc} = N \times \Phi = N \times E_P / (\pi r^2) \quad \text{(S2)}$$

where $N$ is determined in Eq. (S1) and $\Phi$ is the single pulse fluence given by $E_P / (\pi r^2)$, while $E_P$ denotes the single pulse energy and $r$ the $1/e^2$ Gaussian beam spot radius. The single pulse energy was varied between 6 and 11 μJ, while the scanning speed ($v$) ranged from 1 to 4 mm/s. Parameter selection was guided by preliminary scanning electron microscope (SEM) analysis to identify conditions yielding to the most homogeneous surface modifications without excessive damage. Based on this study, the accumulated fluence for the treatment of all the investigated samples was fixed at $\Phi_{acc}$ = 12 J/cm$^2$, considering $E_P$ = 11 μJ ($\Phi$ = 0.92 J/cm$^2$) and $N$ = 13 ($v$ = 3 mm/s; $2r$ = 39 μm; $f$ = 1000 Hz).

To ensure the effectiveness of the proposed combined route for the preparation of NiO-based electrocatalysts, repeated experiments were conducted under the same operating conditions for both plasma processing and laser treatment, in order to ascertain the reproducibility of material characteristics.

### *§ S1-3. Chemico-physical characterization*

X-ray diffraction (XRD) measurements were carried out in glancing incidence mode ($\theta_i$ = 1.0°) using a Bruker AXS D8 Advance Plus diffractometer equipped with a Göbel mirror and a CuKα X-ray source (λ = 1.54051 Å), powered at 40 kV and 40 mA.

A Zeiss SUPRA 40 VP apparatus, operating at primary electron beam voltages between 10 and 20 kV, was used for field emission-SEM (FE-SEM) analyses. The mean deposit thickness values were obtained by a statistical image analysis, using the ImageJ® software.[6]

X-ray photoelectron spectroscopy (XPS) and reflection electron energy loss spectroscopy (REELS) measurements were performed with a Thermo Scientific ESCALAB QXi spectrometer, equipped with a monochromatized Al Kα X-ray source (hν = 1486.6 eV), at pressures lower than $10^{-7}$ mbar. The instrument was funded by "Sviluppo delle infrastrutture e programma biennale degli interventi del Consiglio Nazionale delle Ricerche (2019)". Binding energy (BE) values were corrected for charging phenomena by referencing to the adventitious C1s signal at 284.8 eV. Atomic percentages (at.%) were evaluated through peak area integration using ThermoFisher sensitivity factors. Peak fitting was carried out with the KolXPD software, using Gaussian-Lorentzian product functions with fixed ratio between Gaussian and Lorentzian functions. Work function measurements were carried out with the sample biased at −3.0 V.[7, 8]

REELS analyses were carried out with a primary electron beam energy of 1.0 keV.

### *§ S1-4. Electrochemical tests*

Before electrochemical tests, electrical contacts were applied to the target samples using a copper tape attached to an FTO conductive region (Figure 4a in the main paper). The reported current densities were obtained by normalizing the registered currents to the sample geometric area (0.2826 $cm^2$).

Electrochemical tests were carried out using an integrated potentiostatic instrumentation consisting of a Zennium-PRO and a PP212 unit from Zahner GmbH. Measurements were carried out in 1.0 M KOH solutions (pH ≈ 14.0) using FTO-supported NiO systems as working electrodes, whereas a MMO (Hg/HgO) electrode and a Pt coil were used as the reference and counter-electrode, respectively. Linear sweep voltammetry (LSV) traces were recorded at a constant scan rate of 5 $mV \times s^{-1}$. Tafel slopes were obtained by plotting the potential *vs*. RHE against log (current density). Chronoamperometry (CA) analyses were carried out at a fixed bias of 1.60 V *vs*. RHE.

The obtained $E_{RHE}$ values were subjected to *iR* correction according to equation:[9]

$$E\ (V) = E_{RHE}\ (V) - iR \qquad (S3)$$

where *i* is the measured current (in A), and *R* the uncompensated cell resistance, estimated from electrochemical impedance spectroscopy (EIS) as the lowest impedance in the Nyquist plots high-frequency region.[10, 11] The uncompensated sample resistances were comprised between 16 and 18 Ω.

The oxygen evolution reaction overpotential (η) was evaluated using the equation:[11-14]

$$\eta\ (V) = E_{RHE} - 1.23 \qquad (S4)$$

where $E_{RHE}$ and 1.23 are the experimental potential and the E° value for $O_2$ evolution, both expressed in V.

The turnover frequency (TOF) was defined according to the relation:[11, 15, 16]

$$TOF = (j \times A) / (4 \times F \times n) \qquad (S5)$$

where j, *A*, *F*, and *n* denote respectively the current density, the geometric electrode area (see above), the Faraday constant (96485 $C \times mol^{-1}$), and the number of nickel moles [calculated from the deposit mass (≈0.20 mg), measured using a Mettler Toledo XS105 DualRange microbalance], assuming that all metal sites are involved in the OER process.[14]

*§ S2. Chemico-physical and electrochemical characterization*

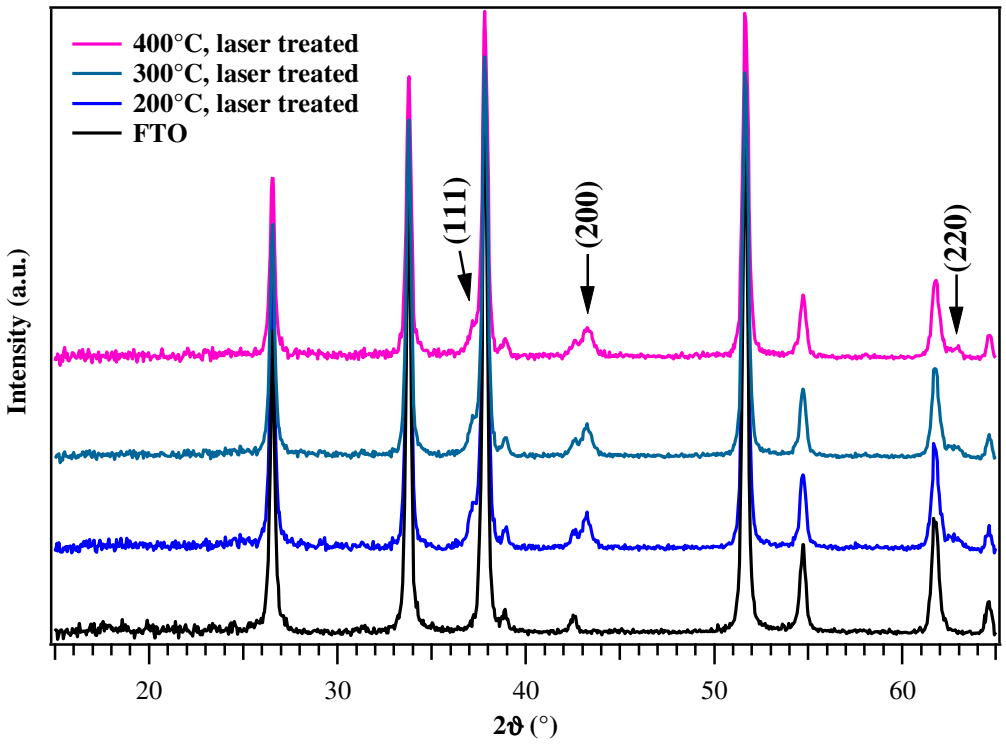


**Fig. S1** XRD patterns for laser-treated specimens. The pattern of the bare FTO substrate (black trace) is superimposed for comparison.

XRD measurements on laser-treated samples yielded the patterns reported in Fig. S1. Beside reflections due to the FTO substrate, peaks at 2θ = 37.2°, 43.3°, and 62.9° were observed and attributed respectively to the (111), (200), and (220) crystallographic planes of cubic NiO.[17] The three specimens featured similar relative peak intensities and comparable crystallite size (≈15 nm, as estimated through the Scherrer equation).

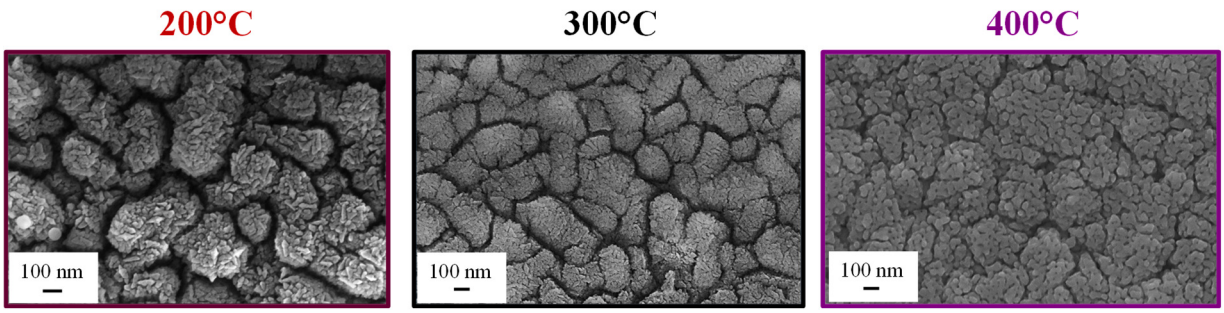


**Fig. S2** Representative plane-view FE-SEM micrographs for NiO specimens deposited at different temperatures before laser treatment.

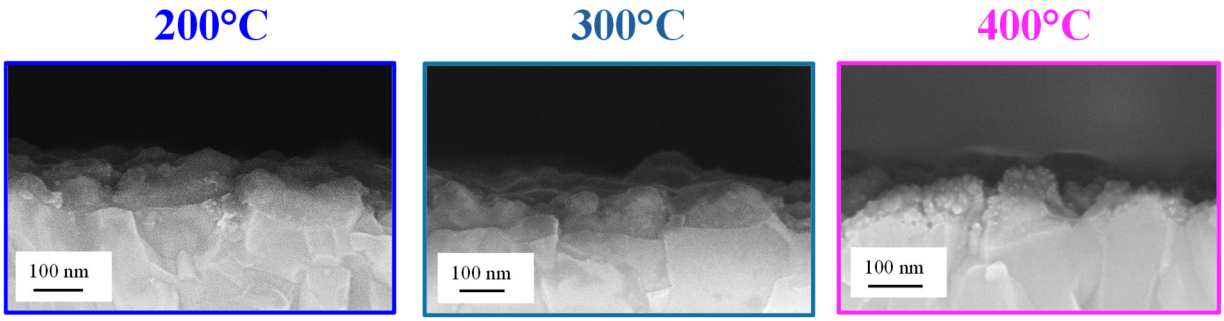


**Fig. S3** Cross-sectional FE-SEM micrographs for laser-treated NiO samples grown at different temperatures.

| $Ni2p_{3/2}$ (200°C) | 1 | 2 | 3 | 4 | 5 |
|---|---|---|---|---|---|
| **BE (eV)** | 854.2 (28.2) | 855.8 (71.8) | 861.3 | 864.2 | 866.9 |
| **FWHM (eV)** | 2.2 | 3.0 | 3.8 | 2.5 | 3.3 |
| | | | | | |
| $Ni2p_{3/2}$ (300°C) | 1 | 2 | 3 | 4 | 5 |
| **BE (eV)** | 854.2 (33.2) | 855.9 (66.8) | 861.4 | 864.3 | 866.9 |
| **FWHM (eV)** | 2.1 | 3.1 | 3.8 | 2.5 | 3.3 |
| | | | | | |
| $Ni2p_{3/2}$ (400°C) | 1 | 2 | 3 | 4 | 5 |
| **BE (eV)** | 853.8 (9.9) | 855.6 (90.1) | 861.1 | 863.9 | 866.6 |
| **FWHM (eV)** | 2.4 | 2.8 | 3.8 | 2.5 | 3.3 |

| O1s (200°C) | NiO | NiO(OH) / $Ni(OH)_2$ | NiO(OH) | NiO-$H_2O_{ads}$ |
|---|---|---|---|---|
| **BE (eV)** | 529.8 (22.3) | 530.8 (39.1) | 531.8 (37.3) | 532.9 (13.2) |
| **FWHM (eV)** | 1.7 | 1.7 | 1.7 | 1.7 |
| | | | | |
| O1s (300°C) | NiO | NiO(OH) / $Ni(OH)_2$ | NiO(OH)/$Ni(OH)_2$ | NiO-$H_2O_{ads}$ |
| **BE (eV)** | 529.8 (23.2) | 530.7 (34.0) | 531.7 (33.6) | 532.8 (10.3) |
| **FWHM (eV)** | 1.7 | 1.8 | 1.9 | 2.2 |
| | | | | |
| O1s (400°C) | NiO | NiO(OH) / $Ni(OH)_2$ | NiO(OH)/$Ni(OH)_2$ | NiO-$H_2O_{ads}$ |
| **BE (eV)** | 530.0 (25.1) | 530.8 (30.1) | 531.8 (24.5) | 532.7 (7.3) |
| **FWHM (eV)** | 1.6 | 1.7 | 1.6 | 1.7 |

**Table S1** BEs and full width at half maximum (FWHM) values of Ni2p and O1s fitting components for laser-treated specimens. The values in parentheses indicate the percentage contribution of each band to the peak area. For the Ni2p signal, the reported values do not include the satellites. The attribution was made basing on previous literature works.[7, 18, 19]

The quantification of the $Ni^{3+}$:$Ni^{2+}$ ratio from the analysis of Ni2p signal is extremely challenging due to the complex and strongly overlapped multiplet envelopes for $Ni^{2+}$ and $Ni^{3+}$.[20] Nevertheless, a semi-quantitative (indirect) estimation of the $Ni^{3+}$ content in the present samples is provided by the deconvolution of the O1s signal and, in particular, by the analysis of the contribution centered at 531.7-531.8 eV, assigned to NiO(OH). As can be observed from data in Table S1, this component revealed an increase of the $Ni^{3+}$ content (and hence of the $Ni^{3+}$:$Ni^{2+}$ ratio) according to the order 400°C < 300°C < 200°C.

| sample | $E_G$ (eV) | IP (eV) | EA (eV) | $E_F$ – VB (eV) |
|---|---|---|---|---|
| **200°C** | 3.0 | 5.8 | 2.5 | 1.5 |
| **300°C** | 3.0 | 5.7 | 2.4 | 1.4 |
| **400°C** | 3.0 | 5.6 | 2.3 | 1.4 |

**Table S2** Energy gap values ($E_G$, estimated by REELS), ionization potential (IP), electron affinity (EA), and valence band edge separation from the Fermi level ($E_F$ – VB) for laser-treated NiO specimens. IP (EA) are evaluated as the energy difference between the valence (conduction) band edges (VB and CB, respectively) and the vacuum level.[7]

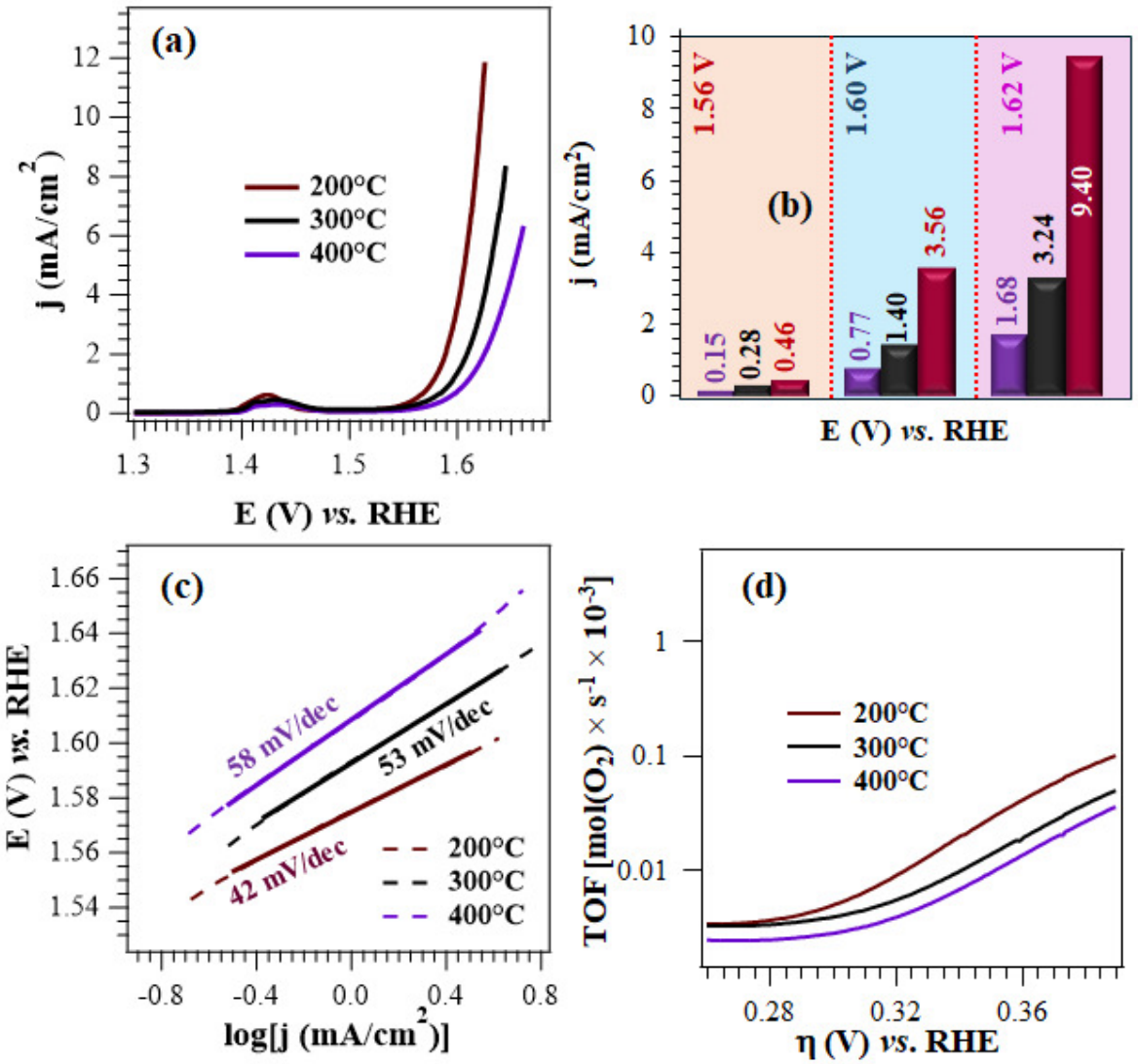


**Fig. S4** (a) LSV traces before laser treatment for FTO-supported specimens. (b) Current densities at different potentials, (c) Tafel plots, and (d) TOF *vs*. overpotential plots for the same samples. In panel (c), dashed and continuous lines correspond to experimental and fitting curves, respectively.

| AS GROWN | | | | | |
|---|---|---|---|---|---|
| **Material** | **Electrolyte** | **j @ 1.60 V (mA/cm$^2$)** | **η @ 10 mA/cm$^2$ (mV)** | **Tafel slope (mV/dec)** | **Ref.** |
| **200°C** | 1.0 M KOH | 3.56 | 390 | 42 | Present work |
| **300°C** | | 1.40 | *n.a.* | 53 | |
| **400°C** | | 0.77 | *n.a.* | 60 | |
| | | | | | |
| **AFTER LASER TREATMENT** | | | | | |
| **Material** | **Electrolyte** | **j @ 1.60 V (mA/cm$^2$)** | **η @ 10 mA/cm$^2$ (mV)** | **Tafel slope (mV/dec)** | **Ref.** |
| **200°C** | 1.0 M KOH | 5.71 | 380 | 40 | Present work |
| **300°C** | | 4.41 | 392 | 43 | |
| **400°C** | | 1.46 | 412 | 46 | |

**Table S3** OER performances of the pristine and laser-treated specimens grown at different temperatures: current density at 1.60 V *vs.* RHE, overpotential (η) required to reach a j value of 10 mA/cm$^2$, and Tafel slopes. *n.a.* = not available.

| Material | Electrolyte | j @ 1.60 V (mA/cm$^2$) | η @ 10 mA/cm$^2$ (mV) | Tafel slope (mV/dec) | Ref. |
|---|---|---|---|---|---|
| **$NiO_x(OH)_y$** | 1.0 M KOH | ≈5.2 | 410 | 75 | [21] |
| **$Ni(OH)_2$** | 1.0 M KOH | ≈1.3 | 420 | 104 | [11] |
| **$Ni(OH)_2$** | 1.0 M KOH | ≈0.8÷4.8 | *n.a.*÷430 | 128÷194 | [22] |
| **$Ni(OH)_2$** | 0.1 M KOH | *n.a.* | 595 | 165 | [23] |
| **$Ni(OH)_2$** | 0.1 M KOH | ≈0.33 | *n.a.* | *n.a.* | [24] |
| **$Ni(OH)_2$** | 1.0 M KOH | ≈10 | ≈370 | 66 | [25] |
| **NiOOH** | 1.0 M LiOH | ≈0.87 | *n.a.* | *n.a.* | [26] |
| **NiOOH** | 0.1 M NaOH | ≈0.20 | *n.a.* | ≈62 | [27] |
| **NiOOH/NiO** | 1.0 M KOH | ≈0.5÷1.5 | ≈510÷550 | ≈70÷170 | [28] |
| **NiO** | 1.0 M NaOH | ≈0.7÷2.9 | 520÷540 | 96÷137 | [29] |
| **NiO** | 1.0 M KOH | ≈1.79 | 460 | 170 | [30] |
| **NiO** | 1.0 M KOH | ≈6.1 | ≈390 | 70 | [31] |
| **NiO** | 1.0 M NaOH | *n.a.* | *n.a.* | 96÷118 | [32] |
| **NiO** | 1.0 M KOH | ≈4.1 | 404 | 97 | [33] |
| **NiO** | 0.1 M KOH | ≈0.48 | ≈553 | ≈30 | [34] |
| **$NiO_x$** | 1.0 M KOH | ≈1.3 | *n.a.* | *n.a.* | [21] |
| **$NiO_x$** | 1.0 M NaOH | ≈0.7÷1.9 | 520 | *n.a.* | [35] |
| **NiO/NF**[a] | 1.0 M NaOH | ≈7.5 | ≈393 | *n.a.* | [36] |
| **NiO/NF**[a] | 1.0 M KOH | ≈16 | 348 | 105.8 | [37] |
| **NiO-NSs**[b] | 1.0 M KOH | ≈10 | 380 | 299 | [38] |
| **NiO-HMs**[1,c] | 1.0 M KOH | ≈2.7÷4.1 | 470÷550 | 188÷290 | [39] |
| **NiO@C**[d] | 1.0 M KOH | ≈19.8 | 340 | 92 | [40] |
| **NiO NPTs**[e] | 1.0 M KOH | ≈1.88 | ≈460 | 113.6 | [14] |

[1] Subjected to thermal treatment in air at 400-500°C.

| Material | Electrolyte | j @ 1.60 V ($mA/cm^2$) | η @ 10 $mA/cm^2$ (mV) | Tafel slope (mV/dec) | Ref. |
|---|---|---|---|---|---|
| **NiO NPTs/GO**[e,f] | 1.0 M KOH | ≈0.85 | 625 | 168 | [41] |
| **Ni/NiO** | 1.0 M KOH | ≈6.0÷26.0 | ≈220÷≈290 | 108÷123 | [16] |
| **NiMn DH**[g] | 0.1 M KOH | ≈0.88 | *n.a.* | *n.a.* | [24] |
| **NiCo DH**[g] | 0.1 M KOH | ≈0.14 | *n.a.* | *n.a.* | [24] |
| **NiCu DH**[g] | 0.1 M KOH | ≈0.23 | *n.a.* | *n.a.* | [24] |
| **NiZn DH**[g] | 0.1 M KOH | ≈0.12 | *n.a.* | *n.a.* | [24] |
| **NiFe LDH**[h] | 0.1 M KOH | ≈2.20 | ≈460 | 62 | [42] |
| | | | | | |
| **$RuO_2$** | 1.0 M KOH | ≈5 | ≈428 | 71 | [22] |
| **$RuO_2$** | 1.0 M KOH | ≈4.7 | 410 | 74 | [43] |
| **$RuO_2$** | 1.0 M KOH | ≈8.9 | 370 | 89 | [44] |
| **$IrO_2$** | 1.0 M KOH | ≈8.6 | 390 | 149 | [45] |
| **$IrO_2$** | 0.1 M KOH | ≈4.9 | 461 | 113 | [46] |
| **$IrO_2$** | 1.0 M KOH | ≈13.9 | ≈350 | 95 | [31] |

**Table S4** OER performances reported in the literature for selected Ni-based electrocatalysts operating in alkaline media. The electrochemical performances of selected $RuO_2$ and $IrO_2$ ones are also reported for comparison. *n.a.* = not available. [a] NF = nickel foam; [b] NSs = nanosheets; [c] HMs = hollow microspheres; [d] NiO@C = carbon-wrapped NiO; [e] NPTs = nanoparticles; [f] GO = graphene oxide. [g] DH = double hydroxide; [h] LDH = layered double hydroxide.

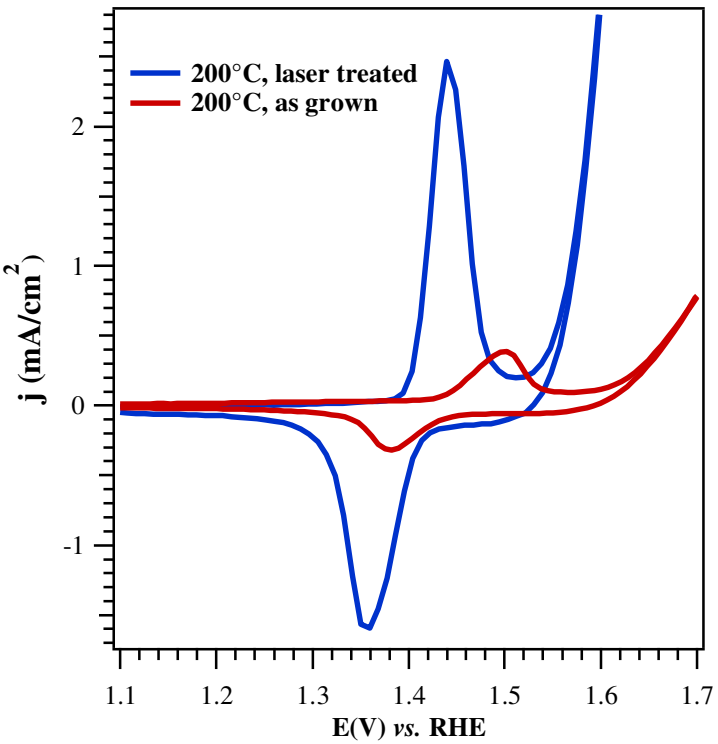


**Fig. S5** Cyclic voltammetry scans (scan rate = 50 mV/s) recorded in 1 M KOH for a laser-treated NiO sample grown at 200°C and the corresponding as grown specimen. The $Ni^{2+}/Ni^{3+}$ oxidation peak above 1.4 V [formation of NiO(OH) during the anodic scan] and the corresponding reduction peak (below 1.4 V, cathodic scan) are well evident.

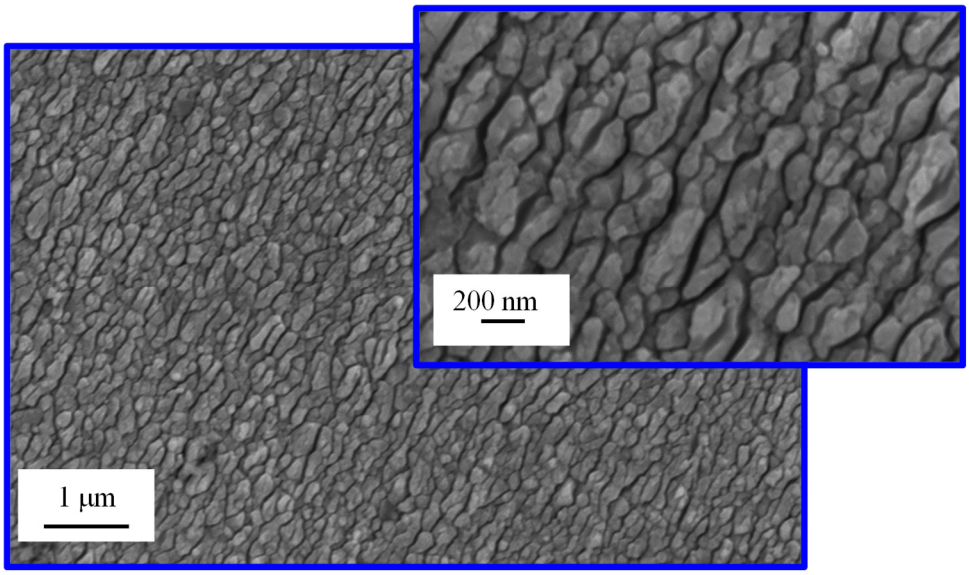


**Fig. S6** FE-SEM images for a laser-treated specimen grown at 200°C, after 12 h of chronoamperometric tests at 1.6 V *vs*. RHE.

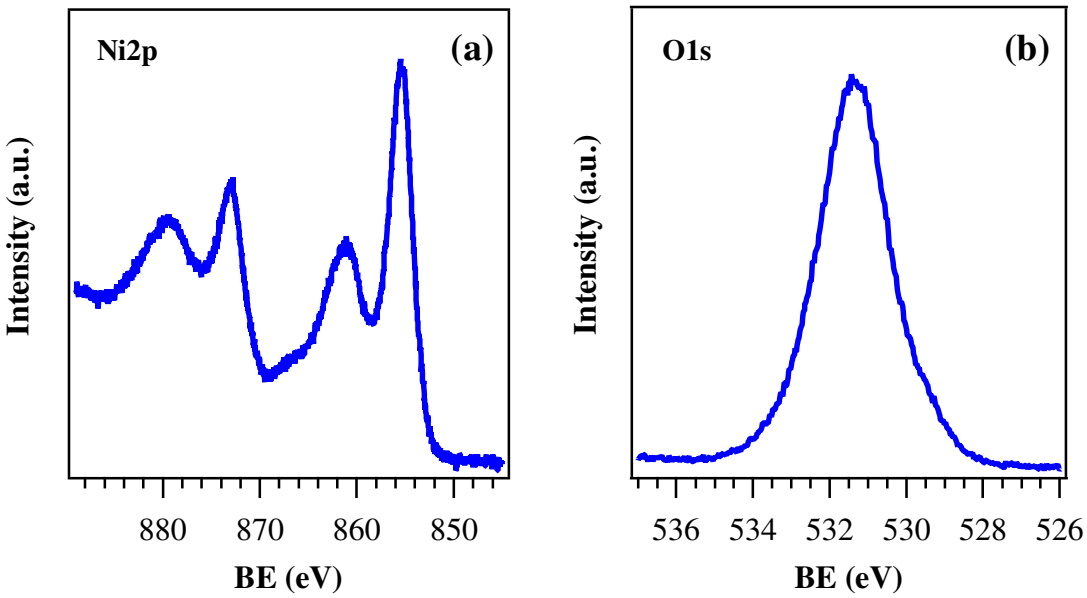


**Fig. S7** (a) Ni2p and (b) O1s photopeaks for a laser-treated NiO sample grown at 200°C after 12 h of chronoamperometric tests at 1.6 V *vs*. RHE.

## *§ S3. References*


1 D. Barreca, G. Carraro, A. Gasparotto, C. Maccato, C. Sada, A. P. Singh, S. Mathur, A. Mettenbörger, E. Bontempi and L. E. Depero, *Int. J. Hydrogen Energy*, 2013, **38**, 14189-14199.

2 G. Carraro, A. Gasparotto, C. Maccato, E. Bontempi, F. Bilo, D. Peeters, C. Sada and D. Barreca, *CrystEngComm*, 2014, **16**, 8710-8716.

3 D. Barreca, A. Gasparotto, E. Tondello, C. Sada, S. Polizzi and A. Benedetti, *Chem. Vap. Deposition*, 2003, **9**, 199-206.

4 M. Benedet, D. Barreca, E. Fois, R. Seraglia, G. Tabacchi, M. Roverso, G. Pagot, C. Invernizzi, A. Gasparotto, A. A. Heidecker, A. Pöthig, E. Callone, S. Dirè, S. Bogialli, V. Di Noto and C. Maccato, *Dalton Trans.*, 2023, **52**, 10677–10688.

5 C. Invernizzi, G. Tabacchi, R. Seraglia, M. Benedet, M. Roverso, C. Maccato, S. Bogialli, D. Barreca and E. Fois, *Molecules*, 2024, **29**, 642.

6 https://imagej.net/ij/.

7 M. Benedet, C. Maccato, G. Pagot, C. Invernizzi, C. Sada, V. Di Noto, G. A. Rizzi, E. Fois, G. Tabacchi and D. Barreca, *J. Phys. Chem. C*, 2023, **127**, 22304-22314.

8 D. Barreca, E. Scattolin, C. Maccato, A. Gasparotto, L. Signorin, N. El Habra, A. Šuligoj, U. L. Štangar and G. A. Rizzi, *Chem. Commun.*, 2025, **61**, 2945-2948.

9 Y. Du, Y. Zhang, X. Pu, X. Fu, X. Li, L. Bai, Y. Chen and J. Qian, *Chemosphere*, 2023, **312**, 137203.

10 T. u. Haq and Y. Haik, *ACS Sustainable Chem. Eng.*, 2022, **10**, 6622-6632.

11 S. Cosentino, M. Urso, G. Torrisi, S. Battiato, F. Priolo, A. Terrasi and S. Mirabella, *Mater. Adv.*, 2020, **1**, 1971-1979.

12 L. Bigiani, D. Barreca, A. Gasparotto, T. Andreu, J. Verbeeck, C. Sada, E. Modin, O. I. Lebedev, J. R. Morante and C. Maccato, *Appl. Catal., B*, 2021, **284**, 119684.

13 C. Maccato, L. Bigiani, L. Girardi, A. Gasparotto, O. I. Lebedev, E. Modin, D. Barreca and G. A. Rizzi, *Adv. Mater. Interfaces*, 2021, **8**.

14 V. D. Silva, T. A. Simões, J. P. F. Grilo, E. S. Medeiros and D. A. Macedo, *J. Mater. Sci.*, 2020, **55**, 6648-6659.

15 M. Benedet, A. Gallo, C. Maccato, G. A. Rizzi, D. Barreca, O. I. Lebedev, E. Modin, R. McGlynn, D. Mariotti and A. Gasparotto, *ACS Appl. Mater. Interfaces*, 2023, **15**, 47368-47380.

16 N. Srinivasa, J. P. Hughes, P. S. Adarakatti, M. C, S. J. Rowley-Neale, A. S and C. E. Banks, *RSC Adv.*, 2021, **11**, 14654-14664.

17 Pattern N° 00-0047-1049, JCPDS, 2000.

18 A. R. Blume, W. Calvet, A. Ghafari, T. Mayer, A. Knop-Gericke and R. Schlögl, *Phys. Chem. Chem. Phys.*, 2023, **25**, 25552-25565.

19 G. Pagot, M. Benedet, C. Maccato, D. Barreca and V. Di Noto, *Surf. Sci. Spectra*, 2023, **30**, 024028.

20 A. P. Grosvenor, M. C. Biesinger, R. S. C. Smart and N. S. McIntyre, *Surf. Sci.* , 2006, **600**, 1771-1779.

21 N. Weidler, J. Schuch, F. Knaus, P. Stenner, S. Hoch, A. Maljusch, R. Schäfer, B. Kaiser and W. Jaegermann, *J. Phys. Chem. C*, 2017, **121**, 6455-6463.

22 N. Hussain, W. Yang, J. Dou, Y. Chen, Y. Qian and L. Xu, *J. Mater. Chem. A*, 2019, **7**, 9656-9664.

23 X. Zhou, Z. Xia, Z. Zhang, Y. Ma and Y. Qu, *J. Mater. Chem. A*, 2014, **2**, 11799-11806.

24 O. Diaz-Morales, I. Ledezma-Yanez, M. T. M. Koper and F. Calle-Vallejo, *ACS Catalysis*, 2015, **5**, 5380-5387.

25 M. Gao, L. He, Z.-Y. Guo, Y.-R. Yuan and W.-W. Li, *ACS Appl. Mater. Interfaces*, 2020, **12**, 443-450.

26 L. Gouda, L. Sévery, T. Moehl, E. Mas-Marzá, P. Adams, F. Fabregat-Santiago and S. D. Tilley, *Green Chem.*, 2021, **23**, 8061-8068.

27 J. D. Michael, E. L. Demeter, S. M. Illes, Q. Fan, J. R. Boes and J. R. Kitchin, *J. Phys. Chem. C*, 2015, **119**, 11475-11481.

28 C. Kuai, Y. Zhang, L. Han, H. L. Xin, C.-J. Sun, D. Nordlund, S. Qiao, X.-W. Du and F. Lin, *J. Mater. Chem. A*, 2020, **8**, 10747-10754.

29 F. Basharat, U. A. Rana, M. Shahid and M. Serwar, *RSC Adv.*, 2015, **5**, 86713-86722.

30 A. QayoomMugheri, AneelaTahira, U. Aftab, M. IshaqAbro, S. R. Chaudhry, L. Amaral and Z. H. Ibupoto, *Electrochim. Acta*, 2019, **306**, 9-17.

31 M. Yang, H. Zhu, Y. Zheng, C. Zhang, G. Luo, Q. Xu, Q. Li, S. Zhang, T. Goto and R. Tu, *RSC Adv.*, 2022, **12**, 10496-10503.

32 E. Arciga-Duran, Y. Meas, J. J. Pérez-Bueno, J. C. Ballesteros and G. Trejo, *Electrochim. Acta*, 2018, **268**, 49-58.

33 T. Zahra, K. S. Ahmad, C. Zequine, R. K. Gupta, A. Guy Thomas and M. Azad Malik, *Sustainable Energy Technol. Assess.*, 2020, **40**, 100753.

34 K. L. Nardi, N. Yang, C. F. Dickens, A. L. Strickler and S. F. Bent, *Adv. Energy Mater.*, 2015, **5**, 1500412.

35 D. Zywitzki, D. H. Taffa, L. Lamkowski, M. Winter, D. Rogalla, M. Wark and A. Devi, *Inorg. Chem.*, 2020, **59**, 10059-10070.

36 Z. Qiu, Y. Ma, G. A. Niklasson and T. Edvinsson, *Physchem*, 2021, **1**, 69-81.

37 Z. Qiu, Y. Ma and T. Edvinsson, *Nano Energy*, 2019, **66**, 104118.

38 R. K. Mishra, V. Kumar, G. J. Choi, J. W. Ryu, S. M. Mane, J. C. Shin and J. S. Gwag, *Mater. Lett.*, 2022, **324**, 132740.

39 A. Mondal, A. Paul, D. N. Srivastava and A. B. Panda, *Int. J. Hydrogen Energy*, 2018, **43**, 21665-21674.

40 Q. Dong, C. Sun, Z. Dai, X. Zang and X. Dong, *ChemCatChem*, 2016, **8**, 3484-3489.

41 S. G. Jo, C.-S. Kim, S. J. Kim and J. W. Lee, *Nanomaterials*, 2021, **11**, 3379.

42 C. Tang, H.-S. Wang, H.-F. Wang, Q. Zhang, G.-L. Tian, J.-Q. Nie and F. Wei, *Adv. Mater.*, 2015, **27**, 4516-4522.

43 D. Das, A. Das, M. Reghunath and K. K. Nanda, *Green Chem.*, 2017, **19**, 1327-1335.

44 Q. Xiao, Y. Zhang, X. Guo, L. Jing, Z. Yang, Y. Xue, Y.-M. Yan and K. Sun, *Chem. Commun.*, 2014, **50**, 13019-13022.

45 L. Jiao, Y.-X. Zhou and H.-L. Jiang, *Chem. Sci.*, 2016, **7**, 1690-1695.

46 H. Sim, J. Lee, T. Yu and B. Lim, *Korean J. Chem. Eng.*, 2018, **35**, 257-262.